Geochemical Perspectives Letters

Spinodal decomposition of supercritical fluid forms melt network in a silicate-H_2O system

Q.X. Wang[1], D.Y. Zhou[1], W.-C. Li[1,2], H.W. Ni[1,2*]

OPEN ACCESS

doi: 10.7185/geochemlet.2119

Abstract

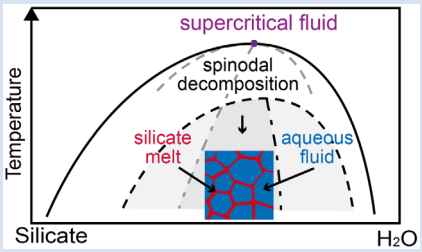

Supercritical fluid in silicate-H_2O systems, with composition intermediate between silicate melt and aqueous fluid, has distinctive physicochemical properties and can be an important agent of mass transfer in Earth's interior. Decreasing temperature and pressure drive supercritical fluid to a miscibility gap and cause unmixing into coexisting melt and fluid. With a hydrothermal diamond anvil cell, we observed that unmixing of a supercritical fluid with 37 to 51 wt. % aluminosilicate formed a silicate melt network, a phenomenon never documented before. The melt network was stable over a range of cooling rates, although further cooling led to disintegration of the network to dispersed melt droplets. The melt network was unlikely to be formed by nucleation-growth at discrete sites, but probably derived from an early stage of spinodal decomposition characterised by high phase interconnectivity. Also key to the stabilisation of melt network was elastic stress supported by polymerised silicate component. The occurrence of a silicate melt network with uneven fluid-melt boundaries may facilitate heterogeneous entrapment of melt and fluid. Spinodal decomposition and formation of melt network provide an efficient mechanism for fluid-melt separation and mineralisation in magmatic-hydrothermal systems.

Received 11 November 2020 | Accepted 15 June 2021 | Published 31 August 2021

Introduction

With increasing pressure and temperature in Earth's interior, the miscibility gap between silicate melt and aqueous fluid diminishes, and single phase supercritical fluid with an intermediate composition (both silicate solute and H_2O are in the range of 30–70 wt. %) can form, most likely in deep subduction zones (Manning, 2004; Frezzotti and Ferrando, 2015; Ni *et al.*, 2017) and in pegmatite systems (Sowerby and Keppler, 2002). Supercritical fluid can be an important agent of mass transfer because it can carry large amounts of elements (Kessel *et al.*, 2005; Schmidt and Poli, 2014) while keeping low viscosity (Audétat and Keppler, 2004). The stability field of supercritical fluids is largely determined by the critical curves of silicate-H_2O systems, which were found by experiments to be generally above 1 GPa with negative *P-T* slopes (Shen and Keppler, 1997; Bureau and Keppler, 1999; Sowerby and Keppler, 2002; Mibe *et al.*, 2007, 2008, 2011). Coexisting melt and fluid inclusions with a wide range of silicate to H_2O ratios in pegmatites (Zajacz *et al.*, 2008) imply that decreasing temperature and pressure (to <700 °C and <1 GPa) can drive supercritical fluid to a miscibility gap, and cause its unmixing into coexisting melt and fluid. Unmixing of supercritical fluid is important for unravelling fluid differentiation and melt/fluid inclusion records in both subduction zone and pegmatite settings, but this unmixing process has not been well documented and understood (all previous experiments focused on mixing of silicate and H_2O and the locus of critical curves). Here, we report some novel results from direct observation of unmixing of supercritical fluid in a silicate-H_2O system at conditions pertinent to peralkaline aluminosilicate systems.

Methods

Experiments (see Supplementary Information for details) were carried out in a Bassett-type hydrothermal diamond anvil cell (HDAC) (Bassett *et al.*, 1993). Sample chamber was initially filled with a piece of sodium aluminosilicate glass ($Na_3AlSi_5O_{13}$ with 1.5 wt. % H_2O), distilled water, and an air bubble, with the mass ratio of silicate to H_2O (S/H) ranging from 0.47–1.69 (32 to 63 wt. % silicate; Table S-1). This peralkaline silicate composition was chosen because its complete miscibility does not require extremely high pressure and temperature that would pose serious challenges to HDAC. This heterogeneous solid-liquid-gas system was homogenised into a supercritical fluid upon heating to ~720 °C and concomitant pressurisation to ~1 GPa. During cooling to ~650 °C with cooling rates of 0.001–2 °C/s, unmixing of supercritical fluid was observed by an Olympus BX53 optical microscope with 20× magnification objective (numerical aperture = 0.25) equipped with a camera recorder. Raman spectra of supercritical fluids, silicate melts and aqueous fluids were collected *in situ* with a Horiba Jobin-Yvon LabRam HR Evolution spectrometer.

1. CAS Key Laboratory of Crust-Mantle Materials and Environments, School of Earth and Space Sciences, University of Science and Technology of China, Hefei 230026, China
2. CAS Centre for Excellence in Comparative Planetology, Hefei 230026, China
* Corresponding author (email: hwni@ustc.edu.cn)

Results

A summary of experimental conditions and results is presented in Table S-1, and the videos of selected experiments are available in Supplementary Information. When a supercritical fluid was subjected to cooling, a variety of phenomena were observed depending on the S/H ratio of the $Na_3AlSi_5O_{13}$-H_2O system. For S/H less than 0.54, silicate melt droplets were nucleated at discrete sites (Fig. 1a,b), followed by droplet growth and coalescence (Fig. 1c,d). When S/H increased to ~0.57, silicate melt droplets formed homogeneously with a high number density (Fig. 1e–h), and the coalescence of droplets became more prominent. For greater S/H such as 0.68, a spectacular network of silicate melt, with multiple threads and nodes, developed during cooling (Fig. 1i–l). Increasing image contrast between silicate melt network and aqueous fluid (both phases are continuous)

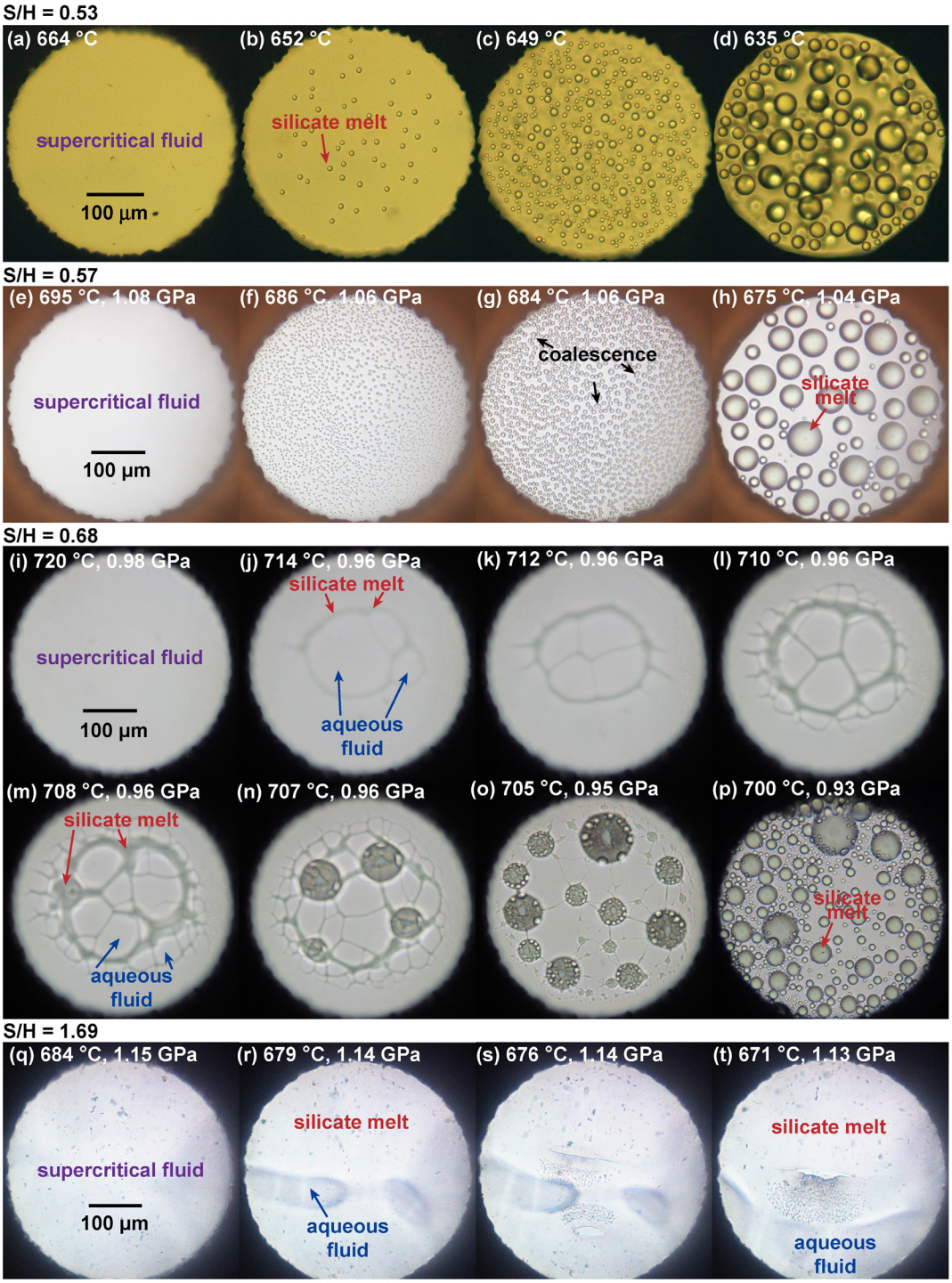

Figure 1 Phenomena observed during cooling and unmixing of supercritical fluid with different silicate to H_2O mass ratios (S/H). **(a–d)** S/H = 0.53, nucleation of silicate melt droplets followed by independent growth. **(e–h)** S/H = 0.57, spinodal decomposition with homogeneously dispersed silicate melt droplets followed by coalescence. **(i–p)** S/H = 0.68, spinodal decomposition and development of a silicate melt network, later disrupted into melt droplets. **(q–t)** S/H = 1.69, spinodal decomposition with large portions of silicate melt and aqueous fluid.

reflected increasing difference in their composition. Melt subsequently retreated toward a number of nodes (Fig. 1m,n), leading to disruption to the network (Fig. 1o). The bicontinuous texture was converted to melt droplets dispersed in the fluid (Fig. 1p). With an increase of S/H from 0.58 to 1.05 (37 to 51 wt. % silicate), melt threads became stronger, alongside less congregation of melt at the nodes (Fig. S-2). At the highest S/H of 1.69 being investigated, instead of a melt network we observed large pockets of aqueous fluid (Fig. 1q–t).

For experimentally practical cooling rates, a silicate melt network always formed as long as the S/H was in the intermediate range of 0.58 to 1.05. When the cooling rate decreased from 2 °C/s to 0.02 °C/s, melt network became sparse, and the size of domains (mainly as pentagonal and hexagonal sections in 2D) increased correspondingly (Fig. 2a–d). Melt network was fairly stable – when cooling rate decreased to 0.001 °C/s, melt network could persist for more than 60 min (Fig. 2e,f). The reversibility of texture evolution is also worth noting: upon heating, dispersed melt droplets reconnected into a network before homogenisation into a supercritical fluid occurred.

Raman spectra of supercritical fluids, silicate melts, and aqueous fluids are presented in Figure 3. For supercritical fluid (Fig. 3a), the band at ~770 cm^{-1}, assigned to the vibration of silica monomers (Zotov and Keppler, 2000), weakened with an increase of S/H from 0.5 to 0.82. Concomitantly, the intensities of the broad bands at 400–700 cm^{-1}, 790–960 cm^{-1} and

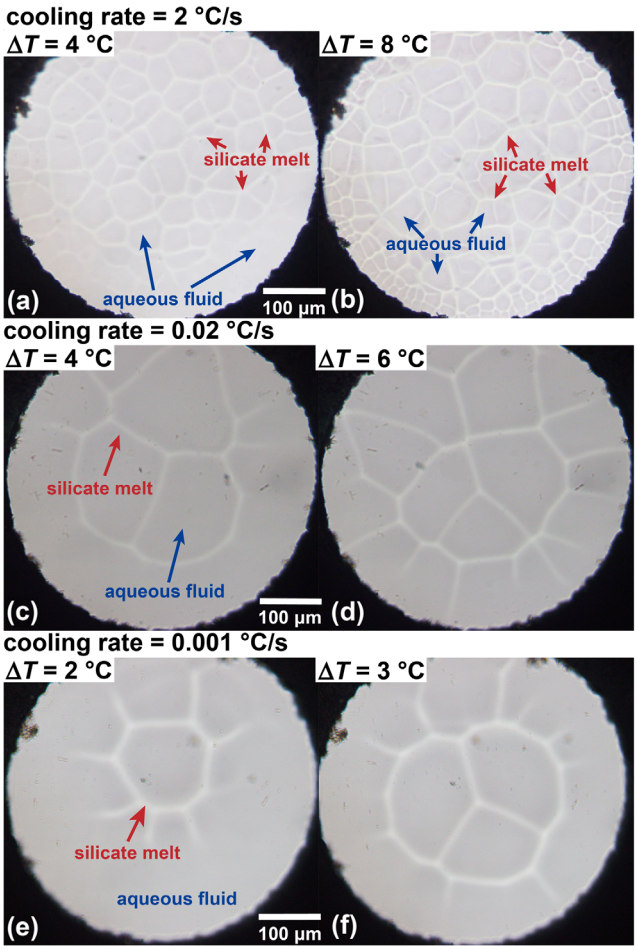

Figure 2 Control of cooling rate on configuration of silicate melt network during spinodal decomposition of supercritical fluid with S/H of 0.92. The ΔT indicates the temperature difference from the point of perceivable unmixing.

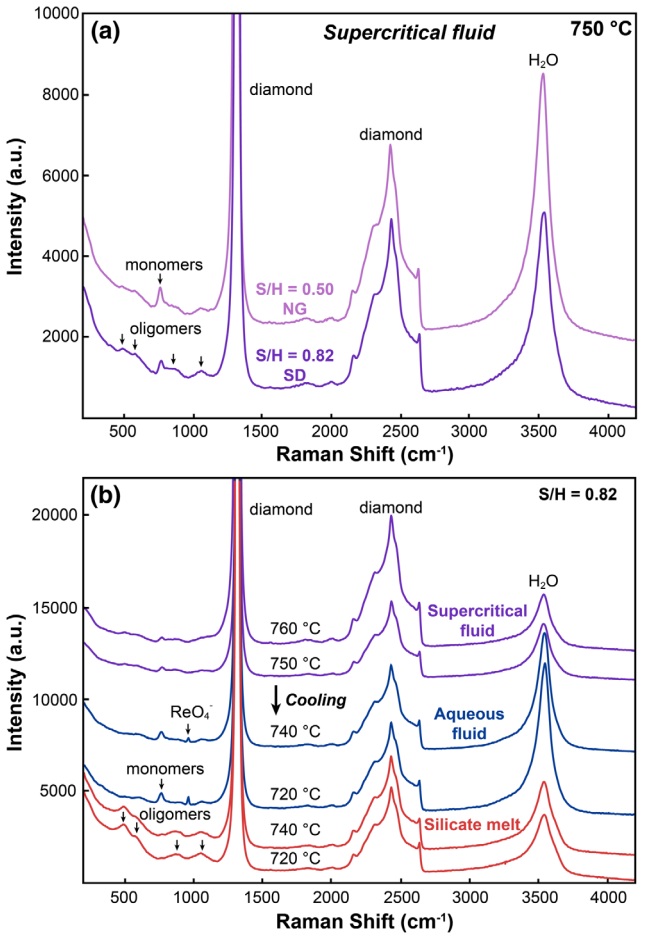

Figure 3 **(a)** Raman spectra of two supercritical fluids at 750 °C, before unmixing by nucleation-growth (NG with S/H = 0.50, light purple) or by spinodal decomposition (SD with S/H = 0.82, purple), respectively. The S/H = 0.50 fluid contained mainly monomers such as H_4SiO_4, whereas the S/H = 0.82 fluid contained more oligomers such as $H_6Si_2O_7$. **(b)** Raman spectra of the supercritical fluid with S/H = 0.82 and coexisting aqueous fluid and silicate melt formed during cooling. The aqueous fluid contained monomers and ReO_4^- (formed by oxidation of the Re gasket), whereas the silicate melt contained more oligomers.

~1050 cm^{-1} (Fig. 3a), related to polymerised aluminosilicate species (*i.e.* dimers and trimers) (Mibe *et al.*, 2008; Dalou *et al.*, 2014), appeared to increase. After unmixing of supercritical fluid with S/H = 0.82, the 770 cm^{-1} band in the spectra of aqueous fluids indicated significant presence of monomers (Fig. 3b). By contrast, the spectra of silicate melts suggested the dominance of polymerised aluminosilicate species.

Discussion

Experimental results demonstrate the primary control of bulk composition, as indexed by the S/H ratio, over the mechanism and process of unmixing of supercritical fluid in silicate-H_2O systems (Fig. 4). A H_2O-rich supercritical fluid with S/H = ~0.5 (composition *A* in Fig. 4) contains predominantly Si and Al monomers (Fig. 3a). Assembling these monomers to clusters would exhaust silicate solute in the local environment, leading to nucleation of silicate melt droplets at discrete sites (Fig. 1a–d). This nucleation-growth mechanism needs to overcome interfacial energy, and is essentially similar to the exsolution of fluid

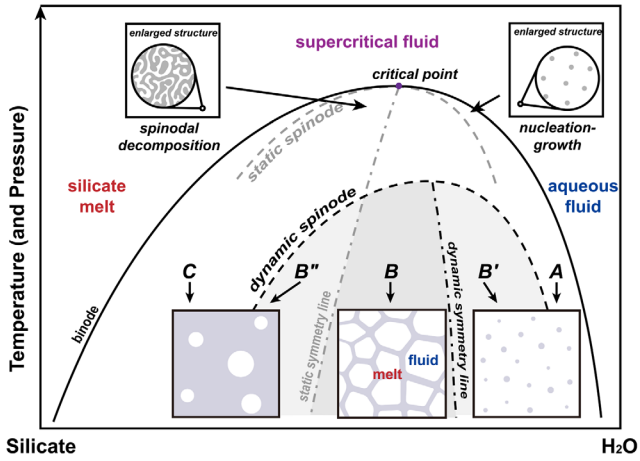

Figure 4 Schematic phase diagram of silicate-H_2O systems including dynamic effects. The binode and the static spinode separate the single phase fluid stability field, the metastable field (nucleation-growth field), and the unstable field (spinodal decomposition field), with a static symmetry line marking equal volumes of silicate melt and aqueous fluid. Unmixing starts either by nucleation (composition *A* and *C*) or by spinodal decomposition (composition *B′*, *B*, and *B″*), but is not visible by optical means. Further cooling produces different patterns of melt-fluid distribution controlled by the dynamic spinode and the dynamic symmetry line. For H_2O-rich composition *B′*, dispersed melt droplets (Fig. 1e–h) are formed, optically similar to composition *A* (Fig. 1a–d). For silicate-rich composition *B″*, aqueous fluid droplets (Fig. 1q–t) appear, optically similar to composition *C*. For composition *B* between the two symmetry lines, a network of silicate melt can be stabilised by elastic stress, before being disintegrated into dispersed melt droplets by interfacial tension (Fig. 1i–p). Explanations are partly based on the theory of viscoelastic phase separation (Tanaka, 1994).

bubbles from a hydrous magma (composition C in Fig. 4), except that the roles of silicate and H_2O are exchanged.

By contrast, the observed melt network for S/H in the range of 0.58–1.05, was unlikely to be formed by nucleation-growth, but probably derived from an early stage of spinodal decomposition throughout the supercritical fluid. According to theories of thermodynamics and phase separation (Cahn, 1965; Debenedetti, 2000), when a homogeneous solution falls between the binode (solvus) and the spinode of a miscibility gap, it would either stay metastable or unmix by nucleating a daughter phase with a different composition. But when the solution falls inside the spinode, concentration fluctuation would lead to spontaneous and uniform unmixing and form a bicontinuous structure with high phase interconnectivity, referred to as spinodal decomposition. The presence of polymerised Si-Al-Na species (Fig. 3a) could facilitate spinodal decomposition of supercritical fluid.

The initial stage of spinodal decomposition was difficult to capture by optical microscope due to the limit on spatial resolution (no better than 2 μm). For S/H = 0.54–0.57 (composition *B´* in Fig. 4), the observation of uniformly distributed melt droplets implies inheritance from spinodal decomposition. Stronger evidence of spinodal decomposition, however, still came from the observation of melt network (composition *B* in Fig. 4), as explained by the theory of viscoelastic phase separation (VPS) for polymer solutions (Tanaka, 1994; Iwashita and Tanaka, 2006).

According to the VPS theory, contrasting dynamics between two components of a binary solution is key to the formation of a network pattern. In a supercritical fluid, the silicate component is polymerised and involves a long relaxation time, whereas H_2O is a small molecule and dynamically fast. This dynamic asymmetry led to a large difference in viscoelastic properties between coexisting silicate melt and aqueous fluid, and a melt network was stabilised by elastic stress induced by the slower silicate component. The approximately 120° angle between silicate melt threads (Fig. 1j–n) supports the existence of stress. For geologically relevant cooling rates of magmatic-hydrothermal systems (of the order of °C/kyr to °C/Myr; Lake, 2013), which are much lower than our experimental values (0.001–2 °C/s), a silicate melt network is expected to be highly stable.

Further cooling enlarged the compositional difference between silicate melt and aqueous fluid and hence interfacial tension. After outweighing the elastic stress, interfacial tension eventually caused disintegration of the melt network, and the structure was relaxed into dispersed melt droplets. In principle, the relaxation rate should be controlled by interfacial tension and melt viscosity (Tanaka and Araki, 2006), although we still lack the essential parameters to verify this relationship quantitatively.

Tanaka (1994) suggested the presence of a dynamic spinode inside the thermodynamic (static) spinode (Fig. 4). A network pattern appears in the region between the static symmetry line (corresponding to equal volumes of silicate melt and aqueous fluid) and the dynamic symmetry line. Both unmixing mechanisms, spinodal decomposition and nucleation-growth, can produce droplets structure, but a melt network is unique to viscoelastic spinodal decomposition involving dynamic asymmetry.

The development of a stable silicate melt network during unmixing of supercritical fluid can have important implications for magmatic-hydrothermal systems. Some granitic pegmatites contain fluid/melt inclusions with a spectrum of silicate to H_2O ratios (Zajacz *et al.*, 2008; Thomas *et al.*, 2012), which could be attributed to heterogeneous entrapment of coexisting silicate melt and aqueous fluid. Compared to a droplets structure with smooth spherical fluid-melt phase boundaries, a silicate melt network with uneven phase boundaries would increase the likelihood of trapping melt and fluid together in different proportions. Furthermore, unmixing by spinodal decomposition and formation of an extensive melt network, in contrast to nucleation of fluid/melt droplets at discrete sites, can promote the efficiency of separating aqueous (hydrothermal) fluid from silicate melt. This, in turn, can contribute to the extraction of metals by hydrothermal fluid, and hence to mineralisation.

Conclusions

Our experimental observations demonstrate that the mechanism and process of unmixing of supercritical fluid in silicate-H_2O systems are primarily controlled by its composition. Spinodal decomposition of supercritical fluid with 37 to 51 wt. % silicate developed into a stable silicate melt network due to elastic stress supported by the polymerised silicate component. The occurrence of silicate melt network could facilitate heterogeneous entrapment of coexisting silicate melt and aqueous fluid, and promote the efficiency of melt-fluid separation and mineralisation in magmatic-hydrothermal systems.

Acknowledgements

Instructive comments from Alexander P. Gysi and an anonymous reviewer significantly improved the manuscript. Discussion with Hans Keppler and Youxue Zhang was beneficial. This work was supported by the National Key R&D Programme of China (2018YFA0702700), the National Natural

Science Foundation of China (41825004, 41721002), and the Fundamental Research Funds for the Central Universities of China (WK3410000013).

Editor: Horst R. Marschall

Additional Information

Supplementary Information accompanies this letter at https://www.geochemicalperspectivesletters.org/article2119.

Cite this letter as: Wang, Q.X., Zhou, D.Y., Li, W.-C., Ni, H.W. (2021) Spinodal decomposition of supercritical fluid forms melt network in a silicate-H_2O system. *Geochem. Persp. Let.* 18, 22–26.

References

Audétat, A., Keppler, H. (2004) Viscosity of fluids in subduction zones. *Science* 303, 513–516.

Bassett, W.A., Shen, A.H., Bucknum, M. (1993) A new diamond anvil cell for hydrothermal studies to 2.5 GPa and from −190 to 1200 °C. *Review of Scientific Instruments* 64, 2340.

Bureau, H., Keppler, H. (1999) Complete miscibility between silicate melts and hydrous fluids in the upper mantle: experimental evidence and geochemical implications. *Earth and Planetary Science Letters* 165, 187–196.

Cahn, J.W. (1965) Phase separation by spinodal decomposition in isotropic system. *The Journal of Chemical Physics* 42, 93–99.

Dalou, C., Mysen, B.O., Foustoukos, D. (2014) In-situ measurements of fluorine and chlorine speciation and partitioning between melts and aqueous fluids in the Na_2O-Al_2O_3-SiO_2-H_2O system. *American Mineralogist* 100, 47–58.

Debenedetti, P.G. (2000) Phase separation by nucleation and by spinodal decomposition: fundamentals. In: Kiran, E., Debenedetti, P.G., Peters, C.J. (Eds.) *Supercritical Fluids*. Nato Science Series E, Volume 366. Springer, Dordrecht, 123–166.

Frezzotti, M.L., Ferrando, S. (2015) The chemical behaviour of fluids released during deep subduction based on fluid inclusions. *American Mineralogist* 100, 352–377.

Iwashita, Y., Tanaka, H. (2006) Self-organisation in phase separation of a lyotropic liquid crystal into cellular, network and droplet morphologies. *Nature Materials* 5, 147–152.

Kessel, R., Schmidt, M.W., Ulmer, P., Pettke, T. (2005) Trace element signature of subduction-zone fluids, melts and supercritical liquids at 120–180 km depth. *Nature* 437, 724–727.

Lake, E.T. (2013) Crystallisation and saturation front propagation in silicic magma chambers. *Earth and Planetary Science Letters* 383, 182–193.

Manning, C.E. (2004) The chemistry of subduction zone fluids. *Earth and Planetary Science Letters* 233, 1–16.

Mibe, K., Kanzaki, M., Kawamoto, T., Matsukage, K.N., Fei, Y., Ono, S. (2007) Second critical endpoint in the peridotite-H_2O system. *Journal of Geophysical Research* 112, B03201.

Mibe, K., Chou, I.M., Bassett, W.A. (2008) In situ Raman spectroscopic investigation of the structure of subduction-zone fluids. *Journal of Geophysical Research* 113, B04208.

Mibe, K., Kawamoto, T., Matsukage, K.N., Fei, Y., Ono, S. (2011) Slab melting versus slab dehydration in subduction-zone magmatism. *Proceedings of the National Academy of Sciences* 108, 8177–8182.

Ni, H., Zhang, L., Xiong, X., Mao, Z., Wang, J. (2017) Supercritical fluids at subduction zones: Evidence, formation condition, and physicochemical properties. *Earth-Science Reviews* 167, 62–71.

Schmidt, M.W., Poli, S. (2014) 4.19 - Devolatilisation during subduction. In: Holland, H.D., Turekian, K.K. (Eds.) *Treatise on Geochemistry*. Second Edition, Elsevier, Amsterdam, 669–701.

Shen, A.H., Keppler, H. (1997) Direct observation of complete miscibility in the albite–H_2O system. *Nature* 385, 68–77.

Sowerby, J.R., Keppler, H. (2002) The effect of fluorine, boron and excess sodium on the critical curve in the albite–H_2O system. *Contributions to Mineralogy and Petrology* 143, 32–37.

Tanaka, H. (1994) Critical dynamics and phase-separation kinetics in dynamically asymmetric binary fluids: New dynamic universality class for polymer mixtures or dynamic crossover? *The Journal of Chemical Physics* 100, 5323.

Tanaka, H., Araki, T. (2006) Viscoelastic phase separation in soft matter: Numerical-simulation study on its physical mechanism. *Chemical Engineering Science* 61, 2108–2141.

Thomas, R., Davidson, P., Beurlen, H. (2012) The competing models for the origin and internal evolution of granitic pegmatites in the light of melt and fluid inclusion research. *Mineralogy and Petrology* 106, 55–73.

Zajacz, Z., Halter, W., Pettke, T., Guillong, M. (2008) Determination of fluid/melt partition coefficients by LA-ICPMS analysis of co-existing fluid and silicate melt inclusions: Controls on element partitioning. *Geochimica et Cosmochimica Acta* 72, 2169–2197.

Zotov, N., Keppler, H. (2000) In-situ Raman spectra of dissolved silica species in aqueous fluids to 900 °C and 14 kbar. *American Mineralogist* 85, 600–604.

Geochemical Perspectives Letters

Spinodal decomposition of supercritical fluid forms melt network in a silicate-H_2O system

Q.X. Wang, D.Y. Zhou, W.-C. Li, H.W. Ni

Supplementary Information

The Supplementary Information includes:

- Materials and Methods
- Table S-1
- Figures S-1 and S-2
- Videos S-1 to S-8
- Supplementary Information References

Materials and Methods

Starting material

Anhydrous $Na_3AlSi_5O_{13}$ glass was prepared from fusing reagent-grade oxides and carbonates at 1200 °C for 24 h followed by quench in water. Hydrous glass was synthesised by sealing distilled water and anhydrous glass powder into a Pt capsule and annealing at 1000 °C and 1 GPa for 24 h in a piston-cylinder apparatus. Water content was determined to be 1.5 wt. % by a PerkinElmer Spotlight 200 microscope attached to a Frontier Fourier-transform infrared spectrometer. Doubly polished hydrous glass sections with a thickness of ~80 μm were prepared for hydrothermal diamond anvil cell (HDAC) experiments.

Hydrothermal diamond anvil cell setup

An externally heated Bassett-type hydrothermal diamond anvil cell (HDAC; Bassett *et al*., 1993) equipped with two type IIa diamonds with a culet size of 1 mm was used in our experiments. Rhenium gasket with an initial thickness of 125 μm and a 400 μm (500 μm for Run#306 and Run#307) pinhole was used to accommodate the sample. Heating was provided by two Pt wire heaters, and temperature was monitored by two type-K thermocouples in direct contact with the diamonds. Because the sample chamber after several cycles of heating and cooling behaved nearly isochoric (Bassett *et al*., 1993), the pressure at a given temperature can be inferred from total fluid density and the equation of state of H_2O (Wagner and Pruß, 2002). This calculation implies small or negligible excess volumes of mixing when water dissolves in the silicate melt or the silicate dissolves in the aqueous fluid. The pressure in one experiment (Run#306) was also estimated by using the Raman shift of zircon band at 1008 cm^{-1} (Schmidt *et al*., 2013). Emission

lines of a Ne lamp were used to calibrate the wavenumber. The uncertainty of pressure estimated from zircon is ±0.05 GPa (Schmidt *et al*. 2013). Comparison between the zircon barometer and calculation base on the equation of state of H_2O indicates that the uncertainty in our pressure estimates is probably of the order of ±0.1 GPa (Fig. S-1).

Calculation of silicate to H_2O mass ratio

The silicate to H_2O mass ratio of each experiment is presented in Table S-1. Before each experiment (except for Run#104), the volume of the cell (sample chamber) was determined with vapour-saturated water only. According to Audétat and Keppler (2005), cell volume (V_{cell}) can be estimated from the size of vapour bubble at a given temperature (V_{vap}), the corresponding densities of vapour and liquid (ρ_{vap} and ρ_{liq}), and the total density of the sample chamber (ρ_{tot}, inferred from vapour-liquid homogenisation temperature) using the following relationship:

$$V_{cell} = \frac{V_{vap} \cdot (\rho_{vap} - \rho_{liq})}{\rho_{tot} - \rho_{liq}} \qquad \text{(Eq. S-1)}$$

In each experiment, V_{vap} was measured at least at five different temperatures for computation of V_{cell}.

In phase separation experiments, the approach above was also used to calculate the fluid accessible volume (*i.e.* excluding the volume of glass) whenever applicable. The total fluid density (also excluding glass) was derived from the homogenisation temperature of water and vapour bubble. The product of fluid accessible volume and total fluid density gives the mass of water. In a few experiments for which the approach above was not applicable, the fluid accessible volume was calculated as the difference between V_{cell} and the volume of glass wafer (see below), and the total fluid density was taken as 1.0 g/cm^3.

The area of silicate glass wafer (A) was measured by optical microscopy (Carl Zeiss Axio Scope.A1). Wafer thickness (h) was measured by a micrometre. Glass density (ρ_{gl}) was estimated to be 2.4 g/cm^3 according to Bagdassarov et al. (2000). The mass of glass wafer is calculated as S. The overall uncertainty of the calculated silicate to H_2O mass ratio is estimated to be ±10 % relative.

***In situ* Raman spectroscopy**

Raman spectra were collected on supercritical fluid, hydrothermal fluid and silicate melt with a Horiba Jobin-Yvon LabRam HR Evolution spectrometer. The acquisition setup involved a 532 nm Nd:YAG laser of 500 mW output power (~55 mW at the sample), a confocal hole of 400 μm diameter, a slit of 100 μm width, an objective of 20 × magnification (numerical aperture = 0.25), a spectral range of 200–4200 cm^{-1} with 600 grooves/mm grating, and a CCD detector (1024 × 256 pixels of 26 × 26 μm). Acquisition time was typically 4 min per spectrum (2 accumulations of 15 s per spectral window).

Supplementary Table

Table S-1 Details of phase separation experiments.

Run	Silicate glass		Water				Silicate to H_2O ratio	Silicate content wt. %	Phase separation mechanism[b]
	volume 10^{-12} m^3	mass µg	V_{liq1}[a] 10^{-12} m^3	V_{liq2}[a] 10^{-12} m^3	density g/cm^3	mass µg			
819[c]	2.84	6.8	14.4		~1.0	14.4	0.47	32	NG
821_1[c]	2.75	6.6	13.2		~1.0	13.2	0.50	33	NG
627_1	3.10	7.4	14.5	14.9	0.985	14.2	0.52	34	NG
104[c]	3.28	7.9	14.9		~1.0	14.9	0.53	35	NG
306	4.59	11.0	19.8	21.8	0.956	20.8	0.53	35	NG
623	3.37	8.1	15.1	15.2	0.984	14.9	0.54	35	SD-D
818[c]	3.16	7.6	14.1		~1.0	14.1	0.54	35	SD-D
626	3.22	7.7	14.0	14.7	0.987	13.8	0.56	36	SD-D/N
622	3.34	8.0	14.4	14.6	0.984	14.2	0.57	36	SD-D
705	3.45	8.3	14.6	13.9	0.987	14.4	0.57	36	SD-D
625	3.31	8.0	13.9	14.7	0.986	13.7	0.58	37	SD-N
621	3.55	8.5	14.4	14.5	0.988	14.2	0.60	38	SD-N
624_2	3.62	8.7	14.4	14.4	0.986	14.2	0.61	38	SD-N
620	3.65	8.8	13.8	14.3	0.977	13.5	0.65	39	SD-N
708	3.63	8.7	14.0	13.7	0.984	13.8	0.63	39	SD-N
527	3.50	8.4	13.4	11.5	0.992	12.4[d]	0.68	40	SD-N
619	3.79	9.1	13.2	13.6	0.974	12.9	0.71	41	SD-N
624_1	4.03	9.7	13.0	14.0	0.991	13.3[d]	0.73	42	SD-N
603_1	3.80	9.1	12.2	11.3	0.988	11.6[d]	0.78	44	SD-N
821_2[c]	4.07	9.8	11.9		~1.0	11.9	0.82	45	SD-N
307[c]	6.50	15.60	16.9		~1.0	16.9	0.92	48	SD-N
629	5.33	12.8	13.6	11.2	0.981	12.5[d]	1.02	51	SD-N
603_2	5.31	12.7	14.7	9.7	0.990	12.1[d]	1.05	51	SD-N
627_2	7.63	18.3	12.5	9.6	0.982	10.8[d]	1.69	63	SD-D

[a] V_{liq1} is the fluid accessible volume calculated from the volume difference between the cell and the glass, and V_{liq2} is the fluid accessible volume directly measured with the aid of a vapour bubble. The latter value is adopted whenever applicable.

[b] NG, nucleation-growth; SD-D, spinodal decomposition forming droplets; SD-N, spinodal decomposition forming a silicate melt network.

[c] Vapour bubble vanished quickly after heating, which prohibits accurate determination of V_{liq2} and fluid density.

[d] Calculated using a fluid accessible volume as the average of V_{liq1} and V_{liq2} due to the large difference between them.

Supplementary Figures

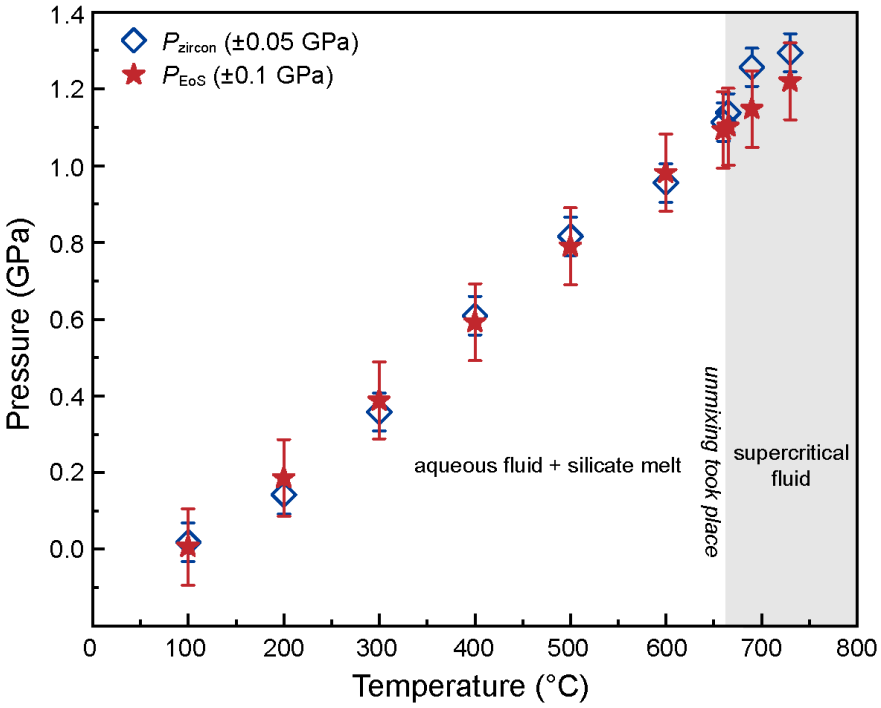

Figure S-1 Variations of pressure with temperature in Run#306, as estimated from the Raman shift of zircon band at ~1008 cm^{-1} (blue diamonds, P_{zircon}; Schmidt *et al*., 2013) and from the EoS of water (red stars, P_{EoS}; Wagner and Pruß, 2002). The uncertainties are ±0.05 GPa for P_{zircon} and ±0.1 GPa for P_{EoS}. Unmixing of supercritical fluid with S/H of 0.53 took place at 664 °C by nucleation-growth.

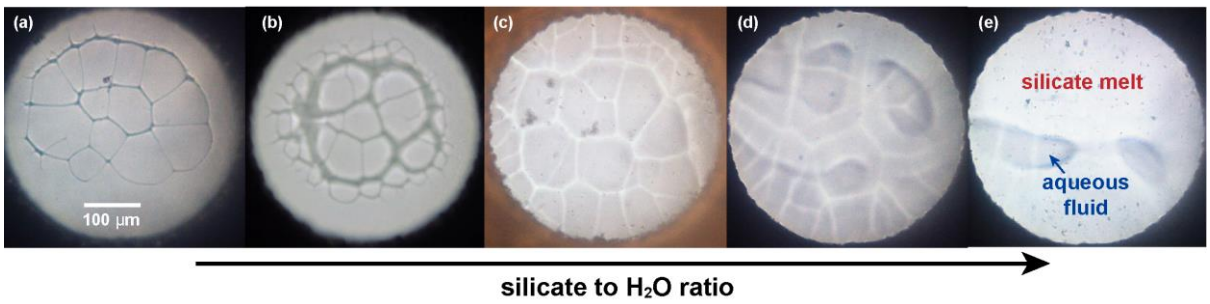

Figure S-2 Silicate to H_2O ratios (by mass) from **(a)** to **(e)** are 0.58, 0.68, 0.73, 1.02 and 1.69, respectively. The network of silicate melt quickly collapsed into melt droplets in **(a)**–**(d)**, whereas the large portions of melt and fluid in **(e)** persisted for long time. The different contrast of images [*i.e.* melt being dark in **(a)** and **(b)** but bright in **(c)**, **(d)** and **(e)**] was due to different focus.

Supplementary Videos

Videos of typical phase separation processes of supercritical fluid

(caption: silicate to H_2O ratio_run number_phase separation mechanism)

Video S-1 0.53_104_NG
Video S-2 0.56_626_SD-DN
Video S-3 0.57_705_SD-D
Video S-4 0.58_625_SD-N
Video S-5 0.63_708_SD-N
Video S-6 0.68_527_SD-N
Video S-7 0.78_603_SD-N
Video S-8 1.69_627_SD-D

The video files are available for download (.GIF files) at https://www.geochemicalperspectivesletters.org/article2119.

Supplementary Information References

Audétat, A., Keppler, H. (2005) Solubility of rutile in subduction zone fluids, as determined by experiments in the hydrothermal diamond anvil cell. *Earth and Planetary Science Letters* 232, 393–402.

Bagdassarov, N., Dorfman, A., Dingwell, D.B. (2000) Effect of alkalis, phosphorus, and water on the surface tension of haplogranite melt. *American Mineralogist* 85, 33–40.

Bassett, W.A., Shen, A.H., Bucknum, M., Chou, I.M. (1993) A new diamond anvil cell for hydrothermal studies to 2.5 GPa and from −190 °C to 1200 °C. *Reviews of Scientific Instruments* 64, 2340–2345.

Schmidt, C., Steele-MacInnis, M., Watenphul, A., Wilke, M. (2013) Calibration of zircon as a Raman spectroscopic pressure sensor to high temperatures and application to water-silicate melt systems. *American Mineralogist* 98, 643–650.

Wagner, W., Pruß, A. (2002) The IAPWS formulation 1995 for the thermodynamic properties of ordinary water substance for general and scientific use. *Journal of Physical and Chemical Reference Data* 31, 387–535.